BIOMATERIALS

Ultraflexible endovascular probes for brain recording through micrometer-scale vasculature

Anqi Zhang[1,2]*, Emiri T. Mandeville[3], Lijun Xu[4], Creed M. Stary[4], Eng H. Lo[3], Charles M. Lieber[2]*†

Implantable neuroelectronic interfaces have enabled advances in both fundamental research and treatment of neurological diseases but traditional intracranial depth electrodes require invasive surgery to place and can disrupt neural networks during implantation. We developed an ultrasmall and flexible endovascular neural probe that can be implanted into sub-100-micrometer–scale blood vessels in the brains of rodents without damaging the brain or vasculature. In vivo electrophysiology recording of local field potentials and single-unit spikes have been selectively achieved in the cortex and olfactory bulb. Histology analysis of the tissue interface showed minimal immune response and long-term stability. This platform technology can be readily extended as both research tools and medical devices for the detection and intervention of neurological diseases.

Neuroelectronic interfaces establish communication between the brain and external devices (*1*–*3*). Many such interfaces have been developed to gather and modulate different forms of neural information, yet there is a clear trade-off between invasiveness and spatial resolution. Nonpenetrating techniques such as electroencephalography (EEG) (*4*) and electrocorticography (*5*) are less invasive but lack the spatial resolution to target individual neurons and are limited to recording from the brain surface. By contrast, invasive approaches such as depth electrodes (*6*–*9*) can achieve single-cell, single-spike resolution in deep brain regions, but open-skull implantation poses considerable risks (*10*), including intracortical bleeding and infection, as well as damage to the targeted brain regions. To overcome the trade-off of invasiveness and resolution, we report an ultraflexible micrometer-scale neuroelectronic interface that uses a native delivery system: the brain vasculature. The metabolically active central nervous system requires a dense vascular network, so the average neuron is less than 20 μm from the nearest blood vessel (*11*, *12*). This vasculature thus offers recording probes access to any brain region without damaging the recorded neural circuits.

Endovascular recording of brain waves in millimeter-scale blood vessels has been demonstrated in previous studies (*13*–*15*). Endovascular EEG in humans (*16*) was first achieved using a guided stainless-steel catheter with a 1.5 mm × 0.6 mm electrode. Through the internal carotid artery (ICA) in the neck, the catheter was advanced to the middle cerebral artery (MCA) in the brain (diameter ~2.9 mm) (*17*). The stentrode™ (Synchron) has an electrode array consisting of eight 0.75-mm electrode discs on a self-expanding stent (*18*, *19*). The stent was inserted through the jugular vein in the neck into the superior sagittal sinus (diameter ~2.4 mm) in sheep. However, much of the brain remains inaccessible with these electrodes because metal-based catheters and stents are stiff and bulky, and navigating them through tortuous brain vasculature with vessels down to the micrometer scale can result in tissue damage and inflammation. Other reports proposed the use of flexible devices to avoid tissue damage. For example, polymer-based wires with a magnetic head can be driven with flow and magnetic steering, demonstrated navigation inside microfluidic devices, and showed endovascular insertion in ex vivo rabbit ears (*20*). However, in vivo endovascular implantation and electrophysiology have not yet been achieved with such flexible devices.

We demonstrate ultraflexible micro-endovascular (MEV) probes that can be precisely delivered through the blood vessels in the neck into sub-100-micrometer scale vessels in rat brains (Fig. 1A). In vivo electrophysiology recording of local field potentials and single-unit spikes has been

[1]Department of Chemical Engineering and Department of Bioengineering, Stanford University, Stanford, CA 94305, USA. [2]Department of Chemistry and Chemical Biology, Harvard University, Cambridge, MA 02138, USA. [3]Neuroprotection Research Laboratory, Departments of Radiology and Neurology, Massachusetts General Hospital and Harvard Medical School, Charlestown, Boston, MA 02129, USA. [4]Department of Anesthesiology, Perioperative & Pain Medicine, Stanford University School of Medicine, Stanford, CA 94305, USA.
***Corresponding authors. Email: aqzhang@stanford.edu (A.Z.); liebercharlesm@gmail.com (C.M.L.)**
†Currently retired.

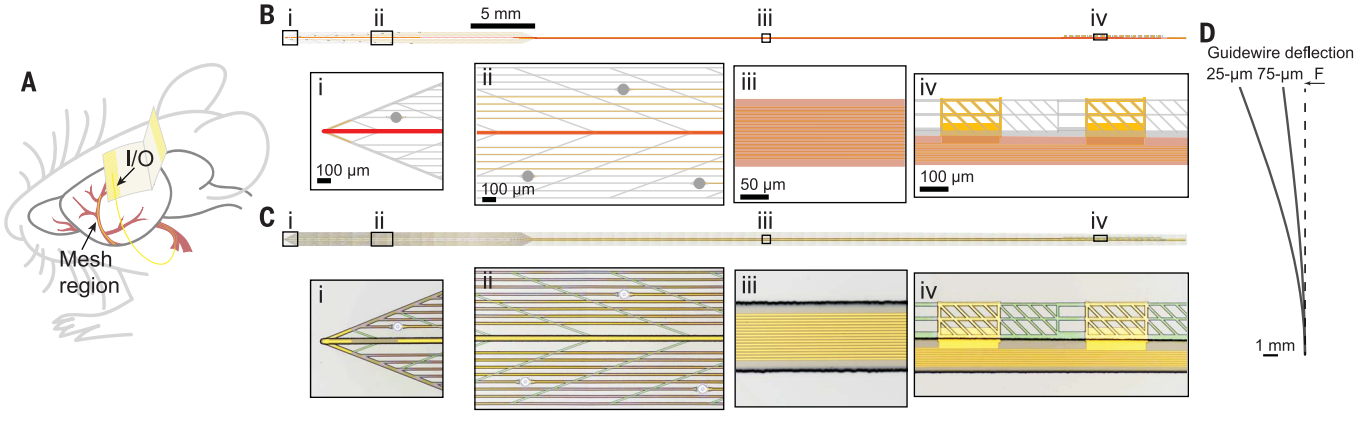

Fig. 1. Endovascular implantation and overview of the MEV probe. (**A**) Schematic showing an MEV probe (yellow) implanted into a rat brain through the blood vessels in the neck. The mesh region with electrodes is implanted in deep cerebrovasculature whereas the input/output (I/O) region remains exteriorized for subsequent connection and measurement. (**B**) Schematic of the MEV probe with the ultraflexible mesh region at left tapering into the stem and I/O region at right. The middle line in red is the thick SU-8 guidewire layer. Insets provide magnified views of (i) probe tip containing the 25-μm wide guidewire (red) and ultraflexible SU-8 mesh region (light gray); (ii) Pt recording electrodes (gray circles); (iii) SU-8 stem containing independent interconnects for each electrode; and (iv) the I/O pads consisting of a gold region (yellow) connected by SU-8. (**C**) Tiled brightfield images of the MEV probe with a 25-μm wide guidewire. The overview and insets are the same size as the schematic regions in (B). The cross-section surface profiles of the probe are shown in fig. S2. (**D**) Side view of the calculated bending of the 18-mm-long guidewire in the device region under the same applied force (F = 10 nN). Deflection of the tip of the 25-μm guidewire probe is 3 times that of the 75-μm guidewire probe (Supplementary Text, fig. S4).

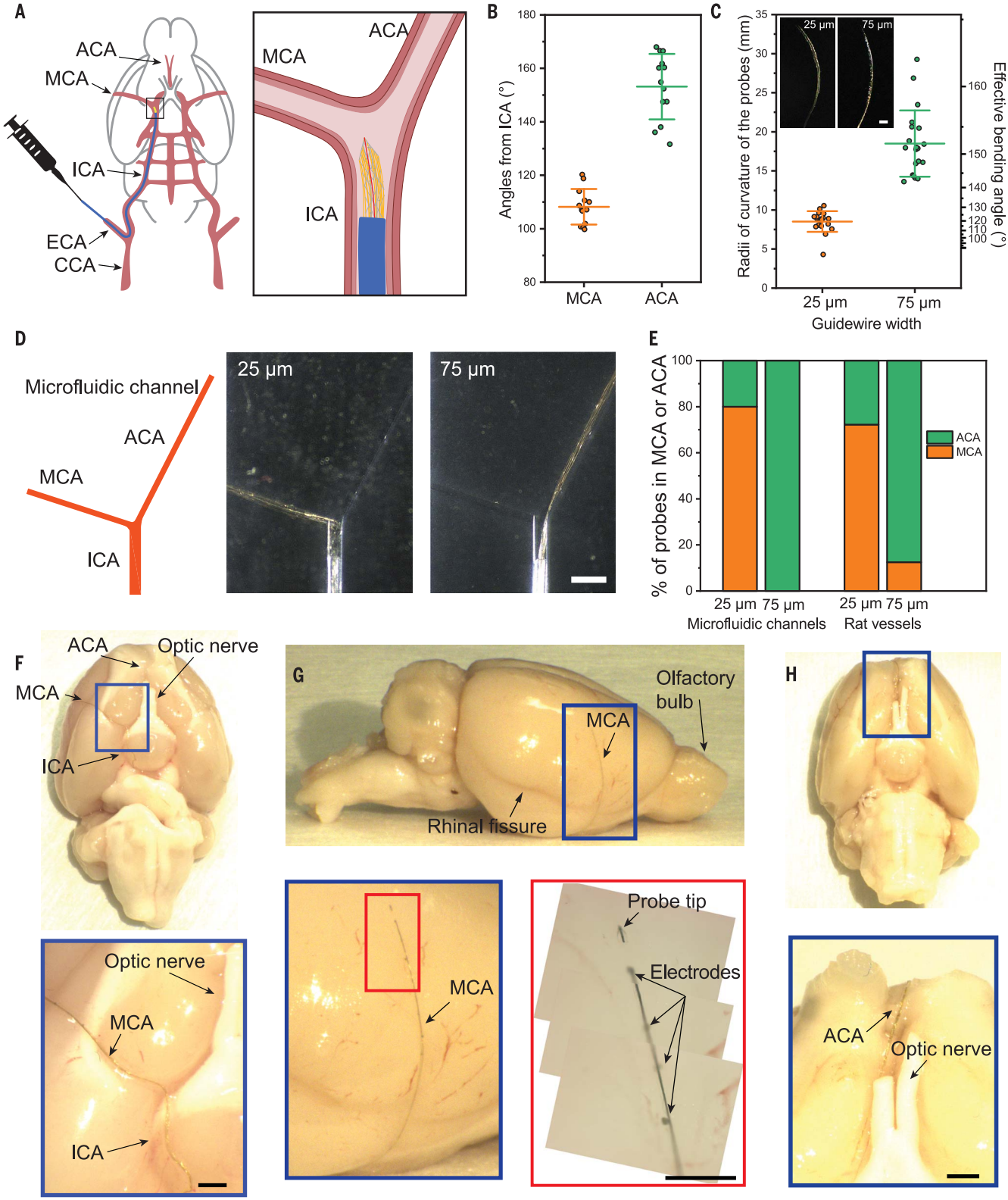

Fig. 2. Branch-selective implantation. (**A**) Schematics of endovascular implantation surgery. A microcatheter loaded with the MEV probe is inserted from the ECA opening to the MCA/ACA bifurcation. Saline carries the probe into the MCA or ACA. (**B**) Angles (n = 13) of the MCAs and the ACAs from the ICAs (with ±1 standard deviation, s.d.) (**C**) Radii of curvature and effective bending angles of the device region (n = 20, with ±1 s.d.) in water. Insets are representative images of the probes with 25-μm and 75-μm guidewires. (**D**) (Left) Schematic of a microfluidic channel designed to mimic the MCA/ACA bifurcation. (Right) Representative implantation of a 25-μm guidewire probe into the MCA channel and a 75-μm guidewire probe into the ACA channel. (**E**) Percentage of probes with different guidewire widths injected into MCA and ACA channels (n = 5 for 25 μm, n = 11 for 75 μm) and rat vessels (n = 18 for 25 μm, n = 8 for 75 μm). (**F**) Inferior and (**G**) sagittal views of dissected rat brains with MEV probes in the MCA. (**H**) Inferior view of a rat brain with a probe in the ACA. Scale bars in all panels are 1 mm.

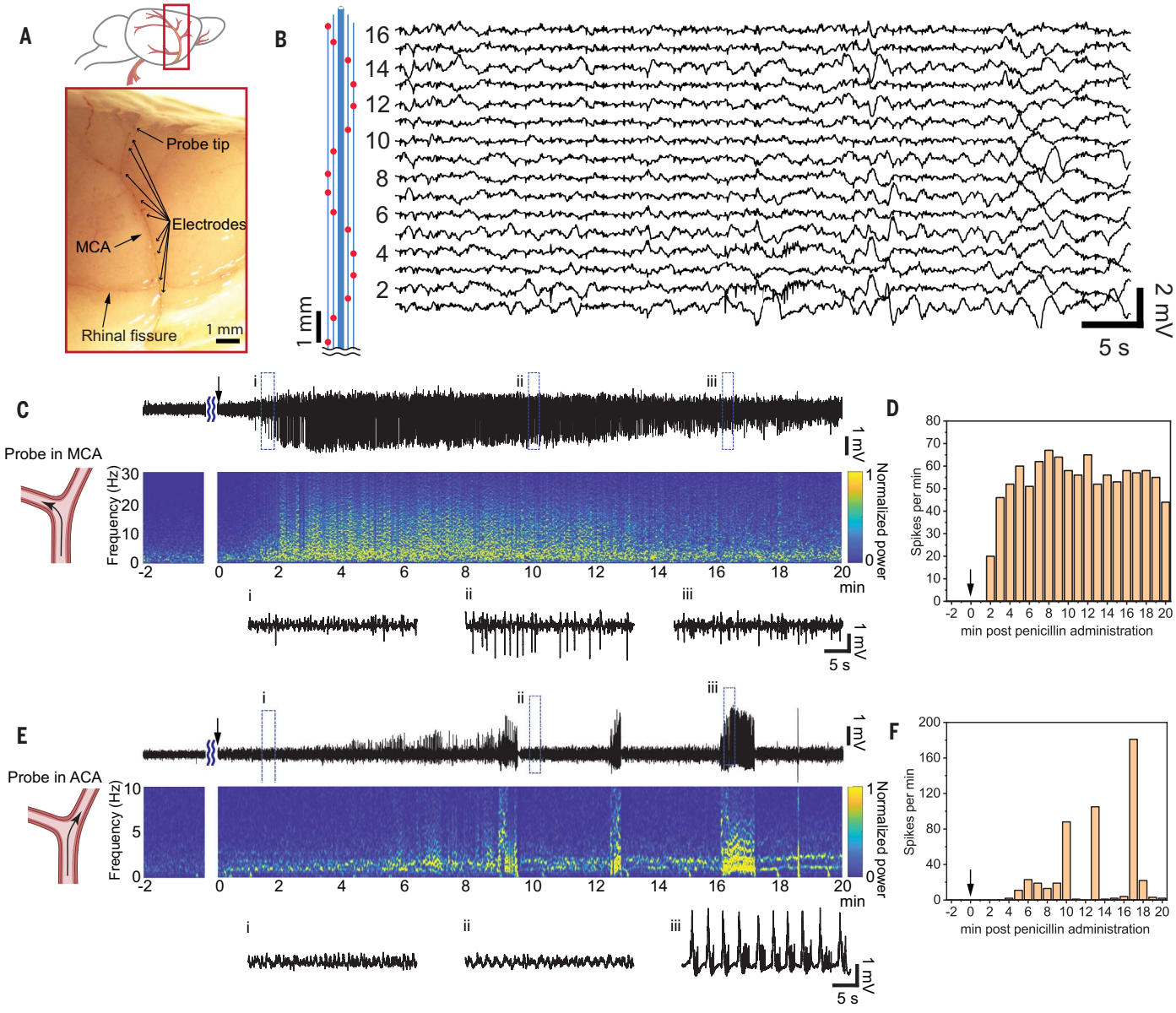

Fig. 3. In vivo endovascular recording. (**A**) Sagittal view of a rat brain showing an MEV probe in the MCA and (**B**) the corresponding acute in vivo 16-channel unfiltered recording showing local field potential oscillations under ketamine/xylazine anesthesia. The relative positions of 16 Pt electrodes are marked by red spots in the schematic in (B) and higher-numbered channels were implanted deeper in the MCA. (**C**) (Top) Penicillin-induced seizures recorded by a representative channel from a probe in MCA for 2 min before and 20 min after penicillin administration. (Middle) spectrogram before and after penicillin administration. The color map shows the normalized power levels of the recording trace. (Bottom) Zoomed-in views showing the evolution of seizure spikes at three different time points. (i to iii) Changes in spike amplitude over time. (**D**) Number of spikes with amplitude over 1 mV per min recorded by the probe in MCA in (C). 1034 spikes were recorded 20 min post administration. (**E** to **F**) Recording and analysis of penicillin-induced seizures from a probe in ACA. (i to iii) show the recording trace before, between, and during burst firing activity. 496 spikes were recorded in 20 min post administration in (F). Black arrows denote the time point of penicillin administration.

selectively achieved in the cortex and olfactory bulb. The flexible probe/vessel wall/brain interface exhibits minimal inflammatory response and long-term stability.

Micro-endovascular probes and their bending properties

We first consider the design of MEV probes and how they meet the key constraints for implantation into the narrow and tortuous sub-100-micrometer-scale brain vascular network without causing damage. Inspired by minimally invasive catheter-based injection procedures (*21*), we design polymer-based ultraflexible MEV probes that can be loaded into and injected from flexible microcatheters. After inserting the microcatheter to the target vessel, the MEV probes are injected into deeper vasculature by saline flow in the microcatheter. The microcatheter is then retracted, leaving the probes in place. This procedure imposes several requirements on the probe design: First, the probes should be able to be loaded into and move smoothly in the microcatheter. Second, the longitudinal bending stiffness of the MEV probes must be sufficient to ensure smooth injection into deeper vasculature beyond the reach of microcatheters without buckling, but also low enough to follow the tortuous vessels and prevent mechanical damage to vessel walls.

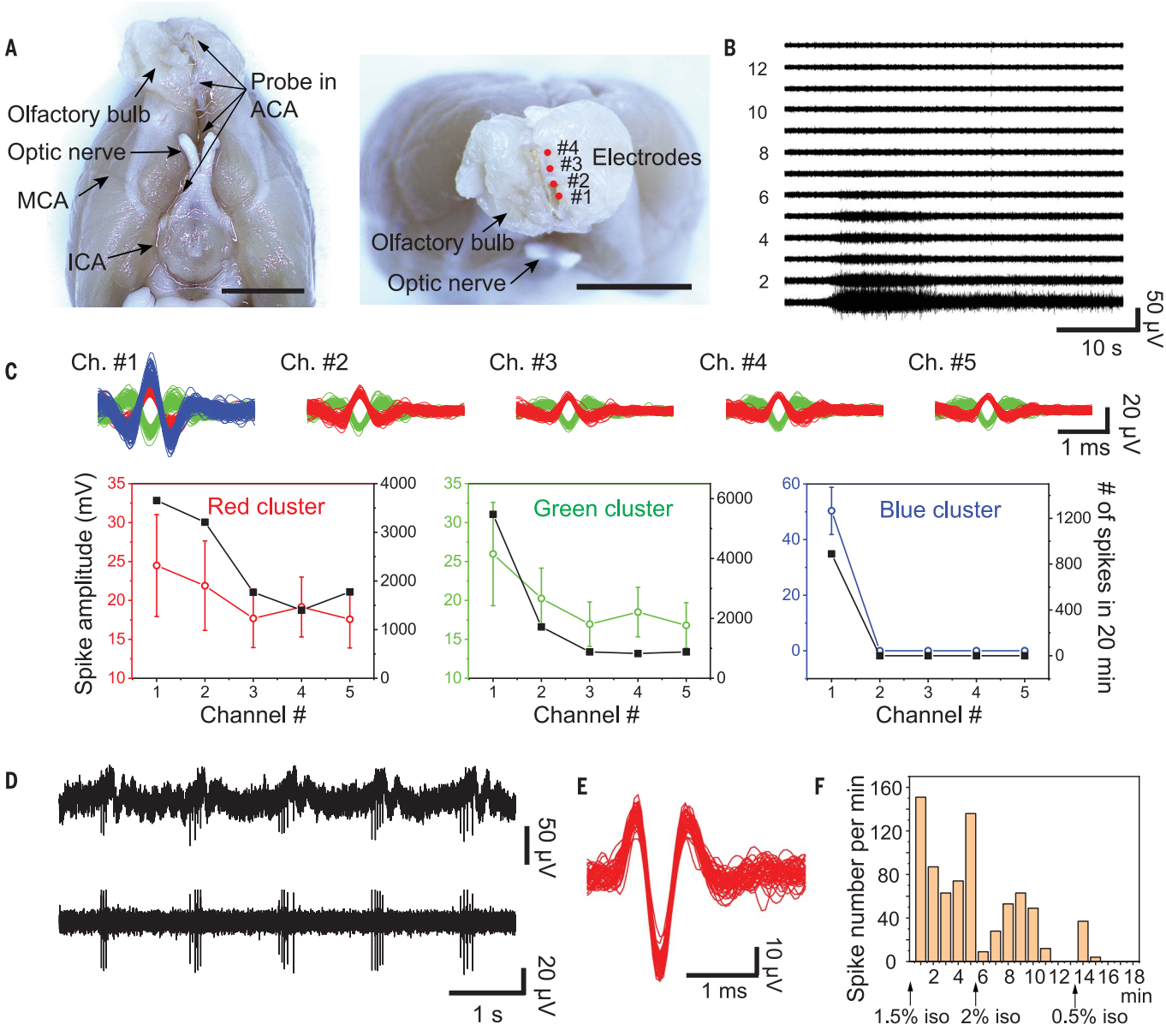

Fig. 4. Single unit recording. (**A** to **B**) Inferior (left) and anterior (right) views of a rat brain with an MEV probe in ACA in (A) the olfactory bulb and (B) the corresponding multichannel recording from the same probe after 250 to 6000 Hz band-pass filtering to show single unit burst activity. Higher-numbered channels were implanted deeper in the ACA. Scale bars in (A) are 5 mm. (**C**) (Top) sorted spikes assigned to different neurons from the channels with single unit activity. Each distinct color in the sorted spikes represents a unique identified neuron. (Bottom) spike amplitude (with ±1 s.d.) and the number of single unit spikes recorded in 20 min. (**D**) Periodic single-unit spikes recorded by a probe in ACA. (Top) the unfiltered recording trace. (Bottom) after 250 to 6000 Hz band-pass filtering. (**E**) Single-unit spikes sorted from the data shown in (D). (**F**) Changes in firing frequency with different isoflurane concentration in which higher concentration (2.0%) decreased and eventually suppressed firing whereas lower concentration (0.5%) temporarily recovered firing.

Third, to optimize recording quality, electrodes on the MEV probes should closely attach to the inner vessel walls (*18*).

The MEV probe (Fig. 1, B and C, and figs. S1 and S2) shows the ultraflexible mesh-like device region on the left, tapering into the flexible stem in the middle, and then to the input/output (I/O) region on the right. In the device region, metal electrodes are embedded in a SU-8 polymer-based mesh-like substrate and are delivered to the targeted brain region, whereas the I/O region remains exteriorized for subsequent connection and measurement. The injection depth can be determined by tracking the location of the I/O region during implantation.

Several aspects of the MEV probe structure have been considered. First, the transverse ribbons in the device region enable the 900-μm-wide probe to be rolled up inside the microcatheter, a flexible tube with an inner diameter of 200 μm and an outer diameter of 350 μm (*22*). Second, an approximately 10-μm-thick guidewire made of SU-8 polymer (Fig. 1B) was designed to optimize longitudinal bending stiffness for smooth injection into tortuous vessel branches without buckling. The guidewire determines the overall bending stiffness of the MEV probe; it was placed over the middle ribbon (other longitudinal ribbons are approximately 0.8 μm thick) in the device region, the stem, and the I/O regions (fig. S2). The bending stiffness of the MEV probes is comparable

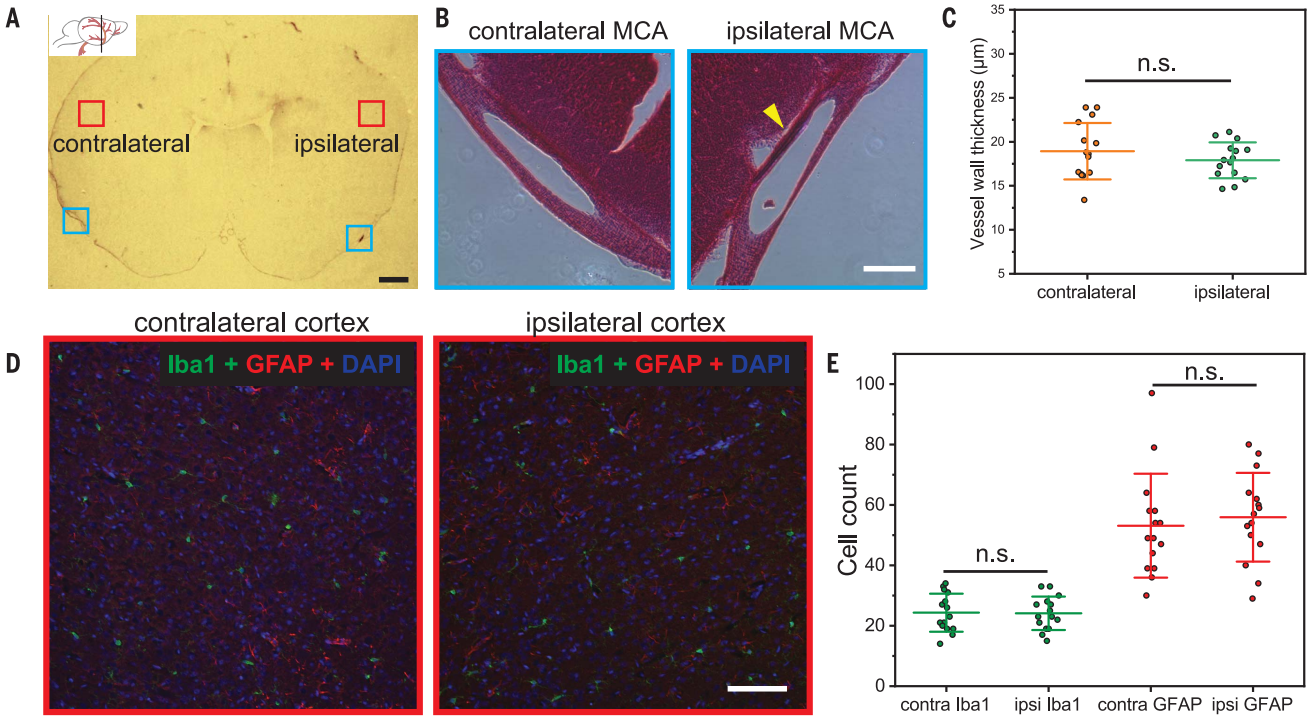

Fig. 5. Chronic histology. (**A**) Optical image of an IgG-stained coronal brain slice 28 days postimplantation in MCA. Scale bar is 1 mm. Inset shows the location of the slice. (**B**) Zoomed-in views of the contralateral and ipsilateral MCAs from Hematoxylin and Eosin (H&E)-stained slices from the regions highlighted by the blue boxes in (A). The yellow arrow highlights the probe embedded in the vessel wall. Scale bar is 100 μm. Note that the vessels were cut at an angle to the central axis; the vessel diameter is the minor axis of the oval cross-section. (**C**) MCA vessel wall thickness with ±1 s.d. measured from similar H&E-stained images as shown in (B). (**D**) Fluorescence microscopy images from the regions highlighted by the red boxes in (A). The brain slices were stained for Iba1 (green) and GFAP (red), and DAPI (blue). Scale bar is 100 μm. (**E**) Number of microglia (Iba1) and astrocytes (GFAP) within 600 μm × 450 μm regions, with ±1 s.d. Results in (C) and (E) were measured from 15 brain slices from three rats (n = 5 for each rat, brain slices from the same rat are 600 μm apart.) n.s., nonsignificant; unpaired two-tailed t-test.

to free-standing 100-μm blood vessels but because the blood vessels are embedded in brain tissue, the vessels will have a larger bending stiffness than the MEV probes (Supplementary Text). The probes were manufactured, released from substrates, and loaded into microcatheters (fig. S3) (*22*–*24*). The probes can advance smoothly within the flexible microcatheter and will remain extended without buckling even when the microcatheter is bent (movie S1). Altering the guidewire width can modify the deflection of the probe tip under a given applied force (Fig. 1D and fig. S4; Supplementary Text). Third, the mesh-like structure relaxes and unfolds after injection (*22*) (fig. S3B and movie S2), allowing the electrodes to adhere against the inner vessel walls, in a similar manner to vascular stent deployment. The rest of the probe is subsequently injected from the microcatheter (fig. S3C). In the device region, 16 platinum electrodes (80 μm each) are distributed over a length of 1 cm, allowing probing of multiple brain regions.

Branch-selective implantation

To demonstrate endovascular implantation, we exploited the established surgical procedure used for rodent stroke models, middle cerebral artery occlusion (MCAO) (*25*), without introducing an occlusion. The common carotid artery (CCA) bifurcates into the external carotid artery (ECA) and ICA in the neck. The ICA segment in the brain branches to form two major cerebral arteries, the MCA and the anterior cerebral artery (ACA), which overlay the cortex and the olfactory bulb, respectively. To perform MCAO, a filament is inserted into the ECA and threaded through the ICA until it occludes the MCA/ACA bifurcation. Similarly, a microcatheter loaded with an MEV probe and attached to a syringe can be inserted into the MCA/ACA bifurcation and the probe subsequently injected (Fig. 2A and fig. S5). Whereas the microcatheter can only reach the MCA/ACA bifurcation, the saline flow in the microcatheter allows the probe to be carried much deeper into either MCA or ACA branches. Following injection, the microcatheter is retracted, leaving the MEV probe in the MCA or ACA.

We achieve branch-selective implantation by tuning mechanical properties of the probe. Because the MCA and the ACA branches are at different angles from the ICA, we sought to determine whether changing the bending angle and bending stiffness of the guidewire would enable selective targeting of MCA and ACA branches. The angles of MCA and ACA from ICA (n = 13, each) were measured to be 108 ± 7° and 153 ± 12°, respectively (Fig. 2B). To match the bending angles of MCA and ACA, we fabricated MEV probes with guidewire widths of 25 μm and 75 μm, respectively. As a result of the residual stress in the SU-8 film generated during processing (*26*, *27*), the device region of the free-standing 25-μm and 75-μm guidewire probes formed radii of curvature of 8.5 ± 1.3 mm and 18.5 ± 4.2 mm in water, respectively (n = 20) (Fig. 2C and fig. S6), which correspond to effective bending angles of 119° and 152°. To test the branch selectivity in vitro, we fabricated polydimethylsiloxane microfluidic channels matching the diameters and angles of the proximal segments of the ICA, MCA, and ACA (Fig. 2D). Microcatheters carrying 25-μm and 75-μm guidewire MEV probes were inserted into the ICA channel and the probes were manually injected into either the MCA or the ACA channels.

An analysis of the branch selectivity (Fig. 2E) in microfluidic channels shows that 80% (n = 5) of the probes with 25-μm guidewires were injected into the MCA channel whereas 100% (n = 11) of the probes with 75-μm guidewires were injected into the ACA channel. Similar branch selectivity was observed for the MEV probes implanted in rat brains in vivo: 72%

(n = 18) of the probes with 25-μm guidewires were implanted into the MCAs whereas 88% (n = 8) of the probes with 75-μm guidewires were implanted into the ACAs. The inferior/horizontal and sagittal views of the perfused and dissected rat brains confirmed the implantation into the MCA (Fig. 2, F and G) and the ACA (Fig. 2H) branches, where the typical injection depth exceeds 1 cm into the distal segments past the microcatheter opening at the MCA/ACA bifurcation. Magnified views of the brains (Fig. 2, F to H) show that the MEV probes maintain their extended shapes within the targeted vessels without buckling, and the individual electrodes are easily identifiable. In addition, the ultraflexible device region is rolled up within the vessel, squeezing the 80-μm electrodes to the midline, indicating that the inner diameters of the targeted vessels are on the 100-micrometer scale.

In vivo endovascular recording

With probes implanted into the MCA (Fig. 3A, fig. S7) and the ACA of anesthetized rats (fig. S8) we demonstrated the ability of the MEV probes to record brain activity. Representative multichannel recordings (Fig. 3B and fig. S8) yielded well-defined signals across all 16 channels. The fluctuation amplitude (200 μV to 2 mV) and the dominant frequency (<2 Hz) recorded are characteristic of the delta wave local field potentials under ketamine/xylazine anesthesia (*28*).

Following this, we investigated whether the MEV probes implanted in the MCAs covering the cortex and the ACAs covering the olfactory bulb reveal different firing properties of different brain regions in neurological disease models. In anesthetized rats, we created epilepsy models by inducing local seizures with intracortical penicillin injection (*29*, *30*) into the right hemisphere where the probes were implanted (Fig. 3, C and E). Electrophysiological recordings by a representative channel on a probe implanted in the MCA (Fig. 3C) show seizure activity characterized by bilateral spikes and spike-wave complexes. Following penicillin administration, seizures began almost immediately and reached a constant level after about 4 min (Fig. 3, C and D). The mean spike frequency and amplitude from 5 to 20 min were 57 ± 6 per min and 1.95 ± 0.62 mV, respectively. Simultaneous recording from all 16 channels of this probe identified spikes only in three adjacent channels (fig. S9), demonstrating the ability of the MEV probes to locate and track the seizure foci. Recordings from MEV probes in MCAs in two other rats recorded similar firing patterns (fig. S10). In comparison, representative recordings from a probe implanted in the ACA showed a latent phase lasting about 4 min after penicillin administration (Fig. 3, E and F). After seizure onset, a burst-suppression pattern was observed. The burst firing activity around 17 min consists of periodic field potential waves (frequency: 0.88 Hz, peak width: 95.8 ± 20.5 ms, amplitude: 2.89 ± 0.24 mV) followed by a train of fast and narrow spikes (frequency: 14.65 Hz, peak width: 1.9 ± 1.0 ms, amplitude: 0.71 ± 0.24 mV) (Fig. 3E). Seizure recordings from ACAs in two other rats showed similar firing patterns (fig. S11).

Comparing the data recorded in the MCAs and the ACAs reveals several important characteristics. First, the seizure spikes spread to the cortex (MCA territory) faster than the olfactory bulb (ACA territory), suggesting that penicillin-induced seizures start as focal activity, then propagate to other brain regions, inducing generalized seizures (*31*). Second, the seizure activity in the cortex regions was consistent with previous reports of rats treated with intracortical penicillin administration (*29*, *30*). Third, the burst-suppression pattern and the periodic field potential waves followed by spike trains recorded from the probes in ACA were similar to those observed from rat olfactory bulb cells (*32*, *33*).

Single unit activity recording

We examine the possibility of recording single-unit spikes across the blood vessel wall, which has not been achieved using previous endovascular probes as a result of their inability to target micrometer-scale vasculature with thin vessel walls. Typical depth electrodes detect spikes from neurons ~130 μm away (*34*). A 100-μm artery has a vessel wall thickness of ~10 to 20 μm (*35*), which is well within the detection range. From the MEV probes injected deeply into the ACA segment overlaying the olfactory bulb under isoflurane anesthesia (Fig. 4A), we repeatedly recorded discontinuous, prolonged spontaneous bursts of action potentials with spindle shapes lasting for tens of seconds (Fig. 4B), characteristic of olfactory bulb mitral cells of anesthetized rats (*32*, *36*). The recording trace of the channels with the largest amplitude activity exhibits single-unit spikes. Single neuron activity was tracked by clustering the sorted spikes with principal component analysis from the channels with single unit activity (*23*), with three neurons identified from Ch. #1, and two neurons identified from Ch. #2 to Ch. #5 (Fig. 4C, top). All neurons exhibit higher spike amplitude and number of spikes in Ch. #1 and decay from Ch. #2 through Ch. #5, indicating that Ch. #1 is the closest to the spiking neurons (Fig. 4C, bottom). Similar recordings were reproducibly observed from other MEV probes in ACAs (fig. S12). In addition, from another MEV probe injected into the ACA under isoflurane anesthesia, we have observed burst spikes nested onto the respiratory rhythm in the field potential (*37*, *38*) (Fig. 4D). The sharp downward spikes (Fig. 4E) showed a uniform potential waveform with average duration ~1 ms and peak-to-peak amplitude of ~60 μV, characteristic of single-unit action potentials (*23*). We tested modulating neuron firing by raising isoflurane concentration (Fig. 4F) from 1.5% to 2%, which suppressed spiking. Decreasing to 0.5% restored spiking, which eventually disappeared, likely attributable to the prolonged exposure to high-concentration isoflurane (*39*).

Chronic histology

We examined both the short-term and chronic effects of MEV probes. For short-term effects laser doppler flowmetry was used to monitor cerebral blood flow before and immediately after probe injection. Representative laser doppler flowmetry traces of probe implantation in the MCA and the ACA (fig. S13) show that probe implantation does not have a substantial effect on the cerebral blood flow. Immediately after MCA implantation, the blood flow fluctuated between 60 and 140% of the baseline, but the average value remained ~ 100%. The blood flow throughout the implantation processes remained much higher than the laser doppler flowmetry level required to induce stroke, which should be stabilized below 30% of the baseline for 90 min (*40*). On days 1, 3, 7, 14, and 28 after MEV probe implantation, we conducted behavior tests using neurological severity scores (*41*). By day 3, all rats had reached a score of 0, indicating no neurologic deficit. In addition, we performed experiments showing that MEV probes are not able to deform or penetrate the vessel walls (movie S3 and Supplementary Text).

We examined how chronic MEV probe implantation affects blood vessel walls and brain tissue. A histology study of the MCA was performed 28 days after implantation as neointimal formation reaches its maximum 28 days after rat artery stenting, thickening the walls substantially (*42*, *43*), and the rat MCAO models start to recover from ischemic damage after 28 days (*44*). First, the blood–brain barrier (BBB) integrity was evaluated with immunoglobulin G (IgG) staining (*45*). IgG-stained brain slices 28 days after implantation in MCA (Fig. 5A) showed no increase in IgG protein in the ipsilateral hemisphere when compared with the contralateral hemisphere, which confirms that the integrity of the BBB was well-preserved. Second, cross sections of the contralateral and ipsilateral MCAs were examined (Fig. 5B and fig. S14), showing that the targeted vessel diameter is less than 100 μm and that the probe ribbons were embedded in the vessel walls. The vessel wall thicknesses of the contralateral and ipsilateral hemispheres are 18.9 ± 3.2 μm and 17.9 ± 2.0 μm measured from 15 brain slices from three rats (Fig. 5C). On the ipsilateral side, no increase in vessel wall thickness was observed, confirming that MEV implants did not cause neointimal formation, which is commonly observed following vascular stenting

(*42*, *43*). Third, the lateral cerebral cortex within the MCA territory was evaluated with fluorescence microscopy (Fig. 5D). Microglia, astrocytes, and nuclei were identified using antibodies against Iba1 (green), glial fibrillary acidic protein (GFAP, red), and DAPI (blue). The numbers of microglia counted from both hemispheres from 15 brain slices from three rats are 24 ± 6 on the contralateral side and 24 ± 5 on the ipsilateral side, while the numbers of astrocytes are 53 ± 17 on the contralateral side and 56 ± 14 on the ipsilateral side. There was no increase of microglia and astrocytes on the ipsilateral side, indicating that endovascular implantation does not induce a significant immune response. Moreover, short-term histology studies conducted 3 days post-implantation in the MCA (fig. S15) and the ACA (fig. S16), and chronic histology studies of the ICA segment in contact with the microcatheter (fig. S17) also showed no increase in vessel wall thickness or number of immune cells. Our chronic histology results showed a substantial improvement from previously reported stiff endovascular probes, which could induce chronic venous thrombosis and occlusion (*18*). These observations not only demonstrate the minimal invasiveness of the MEV probes, but also indicate major advantages in chronic electrophysiology recording, as the accumulation of glial scar tissue near the brain electrodes is known to cause electrode failure in clinically relevant chronic settings (*46*).

Outlook

This study demonstrated ultraflexible probes that can be delivered into sub-100-micrometer–scale vessels in rodents without open-skull surgery. The probes can be selectively implanted into small vessel branches that are not accessible to any available microcatheters, thus enabling neural recording across vessel walls at single cell resolution. Histology studies of the probe-tissue interface showed minimal immune response and long-term stability.

The cerebrovasculature has a hierarchical structure ranging from large superficial cortical vessels to the microvasculature and capillary beds in the cortex. In the rat brain, 4 to 5% of vessels have a diameter of larger than or approximately equal to 100 μm in diameter (*47*), which could be targeted by the reported MEV probes. It should also be possible to target smaller diameter vessels by reducing the width and/or transverse bending stiffness of the probes. In comparison, endovascular probes reported for humans and sheep have only been able to target the largest vessel, the 2.4-mm-diameter sagittal sinus (*18*).

We believe that this platform technology could be extended to the detection and treatment of many neurological diseases as a research tool and could serve as the foundation for clinical translation of minimally invasive neuroelectronic interfaces.

REFERENCES AND NOTES

1. N. G. Hatsopoulos, J. P. Donoghue, *Annu. Rev. Neurosci.* **32**, 249–266 (2009).
2. D. O. Adewole, M. D. Serruya, J. A. Wolf, D. K. Cullen, *Front. Neurosci.* **13**, 269 (2019).
3. J. Wolpaw, E. W. Wolpaw, *Brain-Computer Interfaces: Principles and Practice* (Oxford Univ. Press, 2012).
4. V. Sakkalis, *Modern Electroencephalographic Assessment Techniques* (Springer, 2015).
5. M. Hirata, T. Yoshimine, in *Clinical Systems Neuroscience*, K. Kansaku, L. G. Cohen, N. Birbaumer, Eds. (Springer, 2015), pp. 83-100.
6. G. Hong, C. M. Lieber, *Nat. Rev. Neurosci.* **20**, 330–345 (2019).
7. L. Luan *et al*., *Neuron* **108**, 302–321 (2020).
8. S. Park *et al*., *Nat. Commun.* **12**, 3435 (2021).
9. Z. Zhao *et al*., *Nat. Biomed. Eng.* **7**, 520–532 (2023).
10. E. Hedegärd *et al*., *J. Neurol. Neurosurg. Psychiatry* **85**, 716–720 (2014).
11. I. G. Gould, P. Tsai, D. Kleinfeld, A. Linninger, *J. Cereb. Blood Flow Metab.* **37**, 52–68 (2017).
12. P. S. Tsai *et al*., *J. Neurosci.* **29**, 14553–14570 (2009).
13. R. K. Sefcik *et al*., *Neurosurg. Focus* **40**, E7 (2016).
14. J. Z. Fan, V. Lopez-Rivera, S. A. Sheth, *Front. Neurosci.* **14**, 432 (2020).
15. B. Thielen *et al*., *J. Neural Eng.* **20**, 011001 (2023).
16. R. D. Penn, S. K. Hilal, W. J. Michelsen, E. S. Goldensohn, J. Driller, *J. Neurosurg.* **38**, 239–243 (1973).
17. J. M. Serrador, P. A. Picot, B. K. Rutt, J. K. Shoemaker, R. L. Bondar, *Stroke* **31**, 1672–1678 (2000).
18. T. J. Oxley *et al*., *Nat. Biotechnol.* **34**, 320–327 (2016).
19. N. L. Opie *et al*., *Nat. Biomed. Eng.* **2**, 907–914 (2018).
20. L. Pancaldi *et al*., *Nat. Commun.* **11**, 6356 (2020).
21. W. Sherman, T. P. Martens, J. F. Viles-Gonzalez, T. Siminiak, *Nat. Clin. Pract. Cardiovasc. Med.* **3** (Suppl 1), S57–S64 (2006).
22. J. Liu *et al*., *Nat. Nanotechnol.* **10**, 629–636 (2015).
23. T.-M. Fu *et al*., *Nat. Methods* **13**, 875–882 (2016).
24. X. Yang *et al*., *Nat. Mater.* **18**, 510–517 (2019).
25. L. Belayev, O. F. Alonso, R. Busto, W. Zhao, M. D. Ginsberg, *Stroke* **27**, 1616–1622 (1996).
26. S. Keller, D. Haefliger, A. Boisen, *J. Micromech. Microeng.* **20**, 045024 (2010).
27. S. Keller, G. Blagoi, M. Lillemose, D. Haefliger, A. Boisen, *J. Micromech. Microeng.* **18**, 125020 (2008).
28. S. Chauvette, S. Crochet, M. Volgushev, I. Timofeev, *J. Neurosci.* **31**, 14998–15008 (2011).
29. M. Ayyildiz, S. Coskun, M. Yildirim, E. Agar, *Epilepsia* **48**, 1388–1395 (2007).
30. M. Yildirim, C. Marangoz, *Brain Res.* **1127**, 193–200 (2007).
31. I. Akdogan, N. G. Yonguc, in *Underlying mechanisms of epilepsy*, F. S. Kaneez, Ed. (InTech, 2011), pp. 269-283.
32. G. Leng, H. Hashimoto, C. Tsuji, N. Sabatier, M. Ludwig, *Physiol. Rep.* **2**, e12021 (2014).
33. C. Martin *et al*., *Front. Neural Circuits* **6**, 1 (2012).
34. A. Marblestone *et al*., *Front. Comput. Neurosc.* **7**, 2013.00137 (2013).
35. M. J. Lew, J. A. Angus, *J. Vasc. Res.* **29**, 435–442 (1992).
36. G. Z. Yu, H. Kaba, H. Saito, K. Seto, *Brain Res. Bull.* **31**, 701–706 (1993).
37. B. N. Cazakoff, B. Y. B. Lau, K. L. Crump, H. S. Demmer, S. D. Shea, *Nat. Neurosci.* **17**, 569–576 (2014).
38. R. C. Gerkin, S. J. Tripathy, N. N. Urban, *Proc. Natl. Acad. Sci. U.S.A.* **110**, 17083–17088 (2013).
39. N. Fujiwara *et al*., *J. Physiol.* **402**, 155–175 (1988).
40. R. Schmid-Elsaesser, S. Zausinger, E. Hungerhuber, A. Baethmann, H.-J. Reulen, *Stroke* **29**, 2162–2170 (1998).
41. J. Chen *et al*., *Stroke* **32**, 1005–1011 (2001).
42. B. Langeveld *et al*., *J. Vasc. Res.* **41**, 377–386 (2004).
43. A. V. Finn *et al*., *J. Vasc. Res.* **39**, 414–425 (2002).
44. S. S. J. Rewell *et al*., *PLOS ONE* **12**, e0171688 (2017).
45. M. J. Haley, C. B. Lawrence, *J. Cereb. Blood Flow Metab.* **37**, 456–470 (2017).
46. V. S. Polikov, P. A. Tresco, W. M. Reichert, *J. Neurosci. Methods* **148**, 1–18 (2005).
47. M.-Q. Zhang *et al*., *Sci. Rep.* **5**, 14982 (2015).

ACKNOWLEDGMENTS

The authors acknowledge Z. Bao at Stanford University and T. J. Zwang at Massachusetts General Hospital for helpful discussions. **Funding:** C.M.L. acknowledges support from Air Force Office of Scientific Research (FA9550-18-1-0469, FA9550-19-1-0246) and the Lieber Research Group. E.H.L. acknowledges support from National Institutes of Health (R01NS099620) and the Leducq Foundation. C.M.S. acknowledges support from National Institutes of Health (R01NS107445). A.Z. acknowledges support from American Heart Association (23POST1018301). This work was performed in part at the Harvard University Center for Nanoscale Systems (CNS); a member of the National Nanotechnology Coordinated Infrastructure Network (NNCI), which is supported by the National Science Foundation under NSF award no. ECCS-2025158. This work was performed in part in the nano@Stanford labs, which are supported by the National Science Foundation as part of the National Nanotechnology Coordinated Infrastructure under award ECCS-2026822. **Author contributions:** Conceptualization: A.Z. and C.M.L. Methodology: A.Z., E.T.M., and L.X. Investigation: A.Z., E.T.M., and L.X. Visualization: A.Z. and C.M.L. Funding acquisition: C.M.L., E.H.L., C.M.S., and A.Z. Project administration: C.M.L., E.H.L., and C.M.S. Supervision: C.M.L., E.H.L., and C.M.S. Writing – original draft: A.Z. and C.M.L. Writing – review & editing: A.Z., C.M.L., E.T.M., L.X., C.M.S., and E.H.L. **Competing interests:** A patent application below has been filed by Harvard and Massachusetts General Hospital related to this work. A.Z., C.M.L., E.T.M., and E.H.L., Systems and Methods for Flexible Micrometer-Scale Endovascular Probes for Neural Recording, 2021, PCT/US2021/045679. **Data and materials availability:** All data are available in the main text or the supplementary materials. **License information:** Copyright © 2023 the authors, some rights reserved; exclusive licensee American Association for the Advancement of Science. No claim to original US government works. https://www.sciencemag.org/about/science-licenses-journal-article-reuse

SUPPLEMENTARY MATERIALS

science.org/doi/10.1126/science.adh3916
Materials and Methods
Supplementary Text
Figs. S1 to S17
Movies S1 to S3
References (*48*–*50*)

Submitted 1 March 2023; accepted 19 May 2023
10.1126/science.adh3916

Ultraflexible endovascular probes for brain recording through micrometer-scale vasculature

Anqi Zhang, Emiri T. Mandeville, Lijun Xu, Creed M. Stary, Eng H. Lo, and Charles M. Lieber

Science, **381** (6655), .
DOI: 10.1126/science.adh3916

Editor's summary

Interfacing of neural devices with the brain enables detailed recording and stimulation, but there is typically a trade-off between the level of invasiveness and the resolution of the device. A. Zhang *et al*. developed a probe consisting of an ultrasmall and flexible electronic mesh loaded onto a flexible microcatheter (see the Perspective by Timko). Because of its size and flexibility, this probe can be implanted into 100-micrometer-scale blood vessels in the brain without requiring open skull surgery and without damaging the brain or vasculature. The authors demonstrated the potential of their device by measuring local field potentials and single-unit spikes in the cortex and olfactory bulb of a rat. The meshes also demonstrated long-term stability with minimal immune response. —Marc S. Lavine